Collisional excitation of HC 3 N by para- and ortho-H 2

Alexandre Faure, François Lique, Laurent Wiesenfeld

Monthly Notices
of the
ROYAL ASTRONOMICAL SOCIETY

MNRAS **460,** 2103–2109 (2016)
Advance Access publication 2016 May 13

doi:10.1093/mnras/stw1156

Collisional excitation of HC_3N by para- and ortho-H_2

Alexandre Faure,[1,2]★ François Lique[3]★ and Laurent Wiesenfeld[1,2]★

[1]*Univ. Grenoble Alpes, IPAG, F-38000 Grenoble, France*
[2]*CNRS, IPAG, F-38000 Grenoble, France*
[3]*LOMC-UMR 6294, CNRS-Université du Havre, 25 rue Philippe Lebon, BP 1123 – F-76063 Le Havre Cedex, France*

Accepted 2016 May 11. Received 2016 May 10; in original form 2016 May 4

ABSTRACT

New calculations for rotational excitation of cyanoacetylene by collisions with hydrogen molecules are performed to include the lowest 38 rotational levels of HC_3N and kinetic temperatures to 300 K. Calculations are based on the interaction potential of Wernli et al. whose accuracy is checked against spectroscopic measurements of the HC_3N–H_2 complex. The quantum coupled-channel approach is employed and complemented by quasi-classical trajectory calculations. Rate coefficients for ortho-H_2 are provided for the first time. Hyperfine resolved rate coefficients are also deduced. Collisional propensity rules are discussed and comparisons between quantum and classical rate coefficients are presented. This collisional data should prove useful in interpreting HC_3N observations in the cold and warm ISM, as well as in protoplanetary discs.

Key words: molecular data – molecular processes – scattering – ISM: molecules.

1 INTRODUCTION

Cyanopolyyne molecules, with general formula $HC_{2n+1}N$ ($n \geq 1$), have been detected in a great variery of astronomical environments, from the Solar system to extragalactic sources. The simplest one, HC_3N (cyanoacetylene) is the most abundant of the family. It has been first detected towards the giant Galactic molecular cloud Sgr B2 by Turner (1971) and in comet Hale-Bopp by Bockelée-Morvan et al. (2000). Because of its low rotational constant and large dipole moment, HC_3N is considered as a very good thermometer and barometer in the ISM. It has been detected in the ground level and in excited vibrational levels, thanks to the presence of low-lying bending modes (below 1000 cm^{-1}). Cyanoacetylene is also an abondant nitrogen bearing species and it has been proposed as a precursor of prebiotic molecules such as cytosine, one of the four nitrogen bases found in DNA and RNA (e.g. Orgel 2002).

In most astrophysical regions where HC_3N is observed, the low frequency of collisions (due to low density) cannot maintain local thermodynamical equilibrium (LTE). This is best exemplified by the natural occurrence of the maser phenomenon (microwave amplification by stimulated emission of radiation) in the $1 \rightarrow 0$ transition at 9.1 GHz, as first observed towards Sgr B2 by Morris et al. (1976). The interpretation of HC_3N emission spectra, in terms of density, temperature and column density, thus requires to solve the equations of statistical equilibrium, which in turn necessitates a good knowledge of the collisional rate coefficients. In the cold and dense ISM, the most abundant colliders are hydrogen molecules and helium atoms. In warmer regions, such as photodissociation regions (PDRs) or comets, electron collisions may also play an important role, due to the large HC_3N dipole (3.7 D) (see e.g. Gratier et al. 2013), as well as hydrogen atoms.

The collisional excitation of HC_3N by He and H_2 was first studied by Morris et al. (1976) using the 'hard-ellipsoid' classical approximation. This pioneering work was soon followed by the first determination of the HC_3N-He potential energy surface (PES), using an approximate 'electron gas' model, combined with Monte Carlo quasi-classical trajectory (QCT) calculations (Green & Chapman 1978). Classical mechanics was employed instead of quantum mechanics due to the difficulty of expanding the PES in terms of Legendre polynomials. Indeed, for such extremely anisotropic interactions (HC_3N is $\sim$ nine bohr long), the Legendre polynomial expansion is very slowly convergent and subject to severe numerical problems, as first discussed by Chapman & Green (1977). These problems were circumvented by a novel approach proposed by Wernli et al. (2007a) who derived the first PES for HC_3N–H_2 (hereafter denoted as W07). These authors were thus able to perform both classical and quantum calculations for HC_3N colliding with para-H_2($j_2 = 0$, where j_2 is the H_2 angular momentum). They provided rate coefficients for the lowest 51 rotational levels of HC_3N ($j_1 = 0$–50, where j_1 is the HC_3N angular momentum) and kinetic temperatures in the range 10–100 K. Quantum results were however restricted to the lowest 16 levels, due to the high computational cost of these calculations. In addition, numerical errors in the implementation of the PES routine were found to introduce small inaccuracies ($\lesssim$20 per cent) in the quantum calculations, as reported by Wernli et al. (2007b).

In this work, the W07 PES is first checked against recent high-resolution spectroscopic measurements of the HC_3N–H_2 complex. It is then employed to derive new rate coefficients for

★ E-mail: alexandre.faure@univ-grenoble-alpes.fr (AF); francois.lique@univ-lehavre.fr (FL); Laurent.Wiesenfeld@obs.ujf-grenoble.fr (LW)

HC_3N colliding with para-$H_2(j_2 = 0)$ and, for the first time, with ortho-$H_2(j_2 = 1)$. The quantum coupled-channel approach is employed for the lowest 31 rotational levels of HC_3N ($j_1 = 0$–30) while the QCT approach is employed for higher levels, up to $j_1 = 37$ which is the highest level below the first excited bending mode ν_7 at 222 cm^{-1}. Hyperfine selective collisional cross-sections are also deduced using the almost exact (but computationally demanding) recoupling method and the infinite-order-sudden (IOS) approximation. In Section 2, the spectra of the HC_3N–H_2 complex is computed and it is compared to experimental data. In Section 3, scattering calculations are described and the procedures used to derive cross-sections and rate coefficients are briefly introduced. Results are presented in Section 4. We discuss in particular the propensity rules and a comparison between quantum and classical rate coefficients is made. Conclusions are summarized in Section 5.

2 INTERACTION POTENTIAL AND BOUND-STATES

All bound-state and scattering calculations presented in the following sections were performed with the W07 PES. This PES is briefly described below. The lowest bound-state rovibrational energy levels supported by the PES are computed and the corresponding HC_3N–H_2 transitions frequencies are compared to the recent experimental results of Michaud, Topic & Jäger (2011).

2.1 Potential energy surface

The W07 PES was computed at the coupled-cluster with single, double, and perturbative triple excitations [CCSD(T)] level of theory with an augmented correlation-consistent triple zeta [aug-cc-pVTZ] basis set for HC_3N and quadruple zeta [aug-cc-pVQZ] for H_2, as described in Wernli et al. (2007a). The molecules were both treated as rigid rotors. Owing to the computational cost of the calculations (HC_3N is a 26 electron system), the angular sampling of the PES was performed by using only five independent H_2 orientations. The resulting five PES were interpolated using a bicubic spline function and the full HC_3N–H_2 interaction potential was reconstructed analytically (Wernli 2006). Due to the steric hindrance caused by the HC_3N rod, a standard spherical harmonics expansion of the full PES, as required by quantum calculations, was not possible (see Chapman & Green (1977)). This problem was solved by Wernli et al. (2007a) using a novel approach called 'regularization'. This technique consists in scaling the PES when it is higher than a prescribed threshold so that the potential smoothyl saturates to a limiting value in the highly repulsive regions of the PES. The 'regularized' PES thus retain only the low energy content of the original PES but it is accurately adapted to low collisional energies, in practice lower than ∼1000 cm^{-1} here. The final spherical harmonics fit includes terms up to $l_1 = 24$ and $l_2 = 2$, resulting in 97 angular functions. Full details can be found in Wernli (2006) and Wernli et al. (2007a).

The equilibrium structure of the HC_3N–H_2 complex is linear with the nitrogen of HC_3N pointing towards H_2 at an intermolecular separation of 9.58 bohr. The corresponding well depth is −193.7 cm^{-1}, which compares well with the PES of Michaud et al. (2011; hereafter M11), also computed at the CCSD(T) level, whose grid minimum is at −188.8 cm^{-1}. When averaged over H_2 orientation (corresponding to para-H_2 in its ground state $j_2 = 0$), the W07 PES has a shallower well of −111.2 cm^{-1}, also in good agreement with the M11 averaged PES minimum of −112.6 cm^{-1}. It should be noted, however, that the calculations of M11 were performed for only three orientations of the hydrogen molecule within the complex and no global fit of the PES was provided by the authors.

2.2 Bound-states

A spectroscopic and theoretical study of the HC_3N–H_2 dimer was reported by M11. The bound-state energies of the complex were computed by these authors using scaled and unscaled versions of their PES. These calculations were performed in two-dimensions (2D) using the Lanczos iterative procedure applied to the averaged M11 PES for para-H_2 and to the three PES (corresponding to the three hydrogen orientation) separately for ortho-H_2. The results were compared with high-resolution microwave spectroscopy measurements. Theoretical and experimental transition frequencies were shown to be in good agreement, within a few per cent or better (see below).

We have also computed the bound-state energies supported by the W07 PES using the coupled-channel approach, as implemented in the BOUND program (Hutson 1994). The full spherical harmonics expansion of the W07 PES was employed with 97 functions. The coupled equations were solved using the diabatic modified log-derivative method. These calculations were performed in four-dimensions (4D) for both para- and ortho-H_2. Both molecules were taken as rigid rotors with the rotational constants $B_0 = 59.322$ cm^{-1} for H_2 and $B_0 = 0.151739$ cm^{-1} for HC_3N. A total of 46 rotational states (i.e. up to $j_1 = 45$) were included in the HC_3N basis set while the two lowest rotational states of para-H_2 ($j_2 = 0$, 2) and ortho-H_2 ($j_2 = 1$, 3) were considered. The calculations were performed with a propagator step size of 0.01 bohr and the other propagation parameters were taken as the default BOUND values.

The transition frequencies in the HC_3N–H_2 complex were deduced from the computed bound-state energies. They are compared to the spectroscopic and theoretical data of M11 in Tables 1 and 2 below. The assignment of the (approximate) quantum numbers

Table 1. Transition frequencies (in MHz) in the HC_3N–para-H_2 complex from experiment, from the calculations of M11 and from these calculations. Deviations from the experiment are also given in per cent.

$J'_{K_aK_c} - J''_{K_aK_c}$	Experiment	Michaud et al.	Error (per cent)	Present	Error (per cent)
$1_{01} - 0_{00}$	8295.5435	8240.0	−0.7	8268.8	−0.3
$2_{12} - 1_{11}$	15 601.6795	15 497.7	−0.7	15 529.2	−0.5
$1_{10} - 1_{01}$		16 248.4		16 139.1	
$2_{02} - 1_{01}$	16 549.1211	16 436.5	−0.7	16 514.4	−0.2
$2_{11} - 1_{10}$	17 521.8267	17 418.2	−0.6	17 510.4	−0.07
$3_{13} - 2_{12}$	23 378.90	23 195.3	−0.8	23 283.7	−0.4
$1_{11} - 0_{00}$		23 518.9		23 429.5	
$3_{03} - 2_{02}$	24 718.7675	24 545.3	−0.7	24 656.7	−0.3
$3_{12} - 2_{11}$		26 100.6		26 242.8	

Table 2. Transition frequencies (in MHz) in the HC_3N–ortho-H_2 complex from experiment, from the calculations of M11 and from these calculations. Deviations from the experiment are also given in percent.

$J'_{K_aK_c} - J''_{K_aK_c}$	Experiment	Michaud et al.	Error (per cent)	Present	Error (per cent)
$1_{01} - 0_{00}$	8117.3520	8257.2	1.7	8031.5	− 1.1
$2_{12} - 1_{11}$	15 210.1951	15 663.6	3.0	14 938.0	− 1.8
$2_{02} - 1_{01}$	16 196.1303	16 485.6	1.8	16 048.1	− 0.9
$1_{10} - 1_{01}$	16 670.9616	18 388.7	10.3	18 366.9	10.2
$2_{11} - 1_{10}$	17 097.2104	17 341.8	1.4	16 855.9	− 1.4
$3_{13} - 2_{12}$	22 803.7703	23 477.0	3.0	22 400.0	− 1.8
$1_{11} - 0_{00}$	23 843.1092	25 806.4	8.2	25 421.1	6.6
$3_{03} - 2_{02}$	24 196.9788	24 655.2	1.9	23 987.6	− 0.9
$3_{12} - 2_{11}$	25 625.2174	25 994.1	1.4	25 270.5	− 1.4

$J_{K_aK_c}$ was performed by M11. These authors reported a set of experimental line frequencies including the splitting into several hyperfine components due to the nuclear spin of the nitrogen atom ($I = 1$). In the tables below, the theoretical line frequencies are compared to the unsplit experimental frequencies of M11. The agreement between these values and the experimental data is within 0.5 per cent (i.e. better than 0.01 cm^{-1}) for HC_3N–para-H_2 and within a few per cent (better than 0.1 cm^{-1}) for HC_3N–ortho-H_2. The corresponding average differences are 0.32 per cent and 4.2 per cent, respectively. This very good agreement is similar, although slightly better, than the (non-scaled) theoretical results of M11. This was expected since the level of *ab initio* theory is similar and the improvement is likely due to the 4D approach. We note that M11 were able to obtain an even better agreement by applying simple scaling techniques (radial shifts) to the M11 PES.

In summary, as observed previously for smaller systems such as CO-H_2 (Jankowski, McKellar & Szalewicz 2012) and HCN-H_2 (Denis-Alpizar et al. 2013), the comparison between spectroscopic and theoretical data for HC_3N–H_2 confirms that van der Waals rigid-rotor PES computed at the CCSD(T) level with large basis sets can be used with confidence for analysing van der Waals complexes spectroscopy.

3 SCATTERING CALCULATIONS

Scattering calculations for HC_3N-H_2 were performed using both quantum and classical approaches. The objective was to obtain cross-sections for all transitions among the first 38 rotational levels of HC_3N, i.e. up to $j_1 = 37$ which lies 213.3 cm^{-1} above $j_1 = 0$ and just below the first excited bending mode ν_7 which opens at only 222 cm^{-1}. In practice, for levels higher than $j_1 = 30$, the basis set necessary for converged quantum calculations would require an excessive number of (open and closed) states, including vibrationally excited states. In addition to the substantial CPU cost, such calculations would require the determination of a flexible, nonrigid-rotor, HC_3N–H_2 PES, which is beyond the scope of this work. For the high-lying levels close to the vibrational threshold ($j_1 = 31$–37), the approximate but efficient classical approach was therefore employed. Details on these scattering calculations are given below.

3.1 Quantum calculations

The scattering quantum calculations were conducted at the full coupled-channel level using the MOLSCAT program (Hutson & Green 1995). The spherical harmonics expansion of the W07 PES, including 97 angular functions, was employed and the coupled differential equations were solved using the hybrid modified log-derivative Airy propagator. Total energies up to 2120 cm^{-1} were considered using a fine grid below 200 cm^{-1} (with increments as small as 0.01 cm^{-1}) for the correct assessment of resonances close to thresholds. The total number of collision energies was 324 for para-H_2($j_2 = 0$) and 344 for ortho-H_2($j_2 = 1$). The highest rotational level of HC_3N in the basis set was $j_1 = 44$ while one single rotational level of H_2 was included for both the para ($j_2 = 0$) and ortho ($j_2 = 1$) modifications. The level $j_2 = 2$ of para-H_2 was neglected because it was found to affect the cross-sections by less than 10–20 per cent on average (see also Wernli et al. 2007b) while the CPU cost was increased by large factors. Thus, at a total energy of 100 cm^{-1}, the number of channels was increased by a factor of ∼6 (exceeding 4000 channels) corresponding to a factor of ∼200 in CPU time. We note that we performed a few high-energy calculations with a basis set $j_2 = 0$, 2 in order to compare the cross-sections for $H_2(j_2 = 2)$ with those for $H_2(j_2 = 1)$, see Section 4.3 below. The neglect of HC_3N levels $j_1 > 44$ was found to change cross-sections by less than a few per cent for all transitions among the first 31 levels of HC_3N. The maximum value of the total angular momentum J used in the calculations was $J = 130$ at the highest collisional energy. The rotational constants were taken as $B_e = 60.853$ cm^{-1} for H_2[1] and $B_0 = 0.151739$ cm^{-1} for HC_3N, as in Wernli et al. (2007a). Finally, convergence was checked as a function of the propagator step size (parameter STEPS) and the other propogation parameters were taken as the default MOLSCAT values.

Rate coefficients were obtained for kinetic temperatures in the range 10–300 K by integrating the product of the cross-section by the velocity over the Maxwell–Boltzmann distribution of velocities at each temperature. Cross-sections and rate coefficients are presented in Section 4 below.

3.2 Classical calculations

The objective of the classical calculations was to provide rate coefficients for all (classically allowed) transitions among the levels $j_1 = 31$–37. Kinetic temperatures were restricted to the range 100–300 K since rate coefficients at lower temperatures are available in Wernli et al. (2007a), where full details on the QCT approach can be found. Briefly, it consists in solving the classical Hamilton equations of motion instead of the Schrödinger equation. In the Monte Carlo QCT approach, batches of trajectories are sampled with random (Monte Carlo) initial conditions and they are analysed through statistical methods. In the canonical formalism employed here, the initial collision energies are selected according to the

[1] This value was used for consistency with our previous calculations. Using $B_0 = 59.322$ cm^{-1} instead of B_e would not modify the cross-sections since a single rotational level of H_2 was included.

Maxwell–Boltzmann distribution of velocities and rate coefficients, instead of cross-sections, are directly obtained (see equations (3) and (4) in Wernli et al. (2007a)). State-to-state rate coefficients are obtained by use of the correspondence principle combined with the bin histogram method for extracting the final j_1 quantum number.

Preliminary calculations had shown that QCT calculations for para-H_2($j_2 = 0$) and ortho-H_2($j_2 = 1$) give very similar cross-sections (Wernli 2006). As in Wernli et al. (2007a), we therefore computed QCT cross-sections for para-H_2($j_2 = 0$) only, using the W07 PES averaged over H_2 orientation and fitted with a bicubic spline function. The classical equations of motion were numerically solved using an extrapolation Bulirsh–Stoer algorithm and numerical derivatives for the potential. The total energy and total angular momentum were checked and conserved up to seven digits, i.e. within 0.01 cm^{-1} for the energy. The maximum impact parameter b_{max} was found to range between 20 and 21 bohr for temperatures in the range 100–300 K. Batches of 10 000 trajectories were run for each initial level $j_1 = 31$–37 and each temperature, resulting in a total of 770 000 trajectories. It should be noted that a particular advantage of the QCT method is that the computational time decreases with increasing collision energy, in contrast to quantum methods. QCT calculations however ignores purely quantum effects such as interference and tunneling, as will be shown below.

3.3 Hyperfine excitation

Due to the presence of a nitrogen atom, the HC_3N molecule possess a hyperfine structure. Indeed, the coupling between the nuclear spin ($I = 1$) of the nitrogen atom and the molecular rotation results in a splitting of each rotational level j_1, into three hyperfine levels (except for the $j_1 = 0$ level). Each hyperfine level is designated by a quantum number F_1 ($F_1 = I + j_1$) varying between $|I - j_1|$ and $I + j_1$. As already discussed (e.g. Faure & Lique 2012; Lanza & Lique 2014, and references therein), if the hyperfine levels are assumed to be degenerate, it is possible to simplify considerably the hyperfine scattering problem. Almost exact hyperfine resolved cross-sections can then be obtained from nuclear spin-free S-matrices using the so-called recoupling approach. This approach requires to store the S-matrices and to compute hyperfine resolved S-matrices by properly combining the nuclear spin-free S-matrices. However, in the case of HC_3N–H_2 collisions, the recoupling approach becomes rapidly prohibitive in terms of both memory and CPU time because of the small rotational constant of the target molecule, i.e. the large number of channels to include.

Alternatively, hyperfine resolved rate coefficients can be directly obtained from rotational rate coefficients using the scaled-infinite-order-sudden limit (S-IOS) method first introduced by Neufeld & Green (1994) in the case of HCl-He collisions and then extended to the hyperfine excitation of linear molecules by para- and ortho-H_2 by Lanza & Lique (2014). This adiabatic method is expected to be reliable at high collision energies and/or for target molecules with small rotational constants so that the rotational period is small compared to the collision time-scale. In practice, the hyperfine rate coefficients (or cross-sections) are obtained by scaling the coupled-channel rotational rate coefficients by the ratio of hyperfine and rotational IOS rate coefficients as follows:

$$k^{S-\mathrm{IOS}}_{j_1,F_1,j_2\rightarrow j_1'F_1',j_2'} = \frac{k^{\mathrm{IOS}}_{j_1F_1,j_2\rightarrow j_1'F_1',j_2'}}{k^{\mathrm{IOS}}_{j_1,j_2\rightarrow j_1',j_2'}} k^{CC}_{j_1,j_2\rightarrow j_1',j_2'}, \quad (1)$$

where $k^{\mathrm{IOS}}_{j_1F_1,j_2\rightarrow j_1'F_1',j_2'}$ and $k^{\mathrm{IOS}}_{j_1,j_2\rightarrow j_1',j_2'}$ can be found in equations (6) and (7) of Lanza & Lique (2014). We note that for quasi-elastic transitions (those with $j_1' = j_1$) no scaling is applied, as explained in Faure & Lique (2012). We note also that equation (1) guarantees that the summed hyperfine rate coefficients are identical to the coupled-channel pure rotational rate coefficients.

The S-IOS approach was applied recently to the HCl–H_2 collisional system (Lanza & Lique 2014). Despite the large rotational constant of HCl, the S-IOS method was found to be accurate to within a factor of 2–3 in the case of collisions with para-H_2($j_2 = 0$) at intermediate and high kinetic energies (>200 cm^{-1}). It was however found to fail by factors larger than 3 in the case of ortho-H_2($j_2 = 1$). As HC_3N is much heavier than HCl and hence more adapted to IOS type methods, one can expect the accuracy of the S-IOS approach to be substantially better.

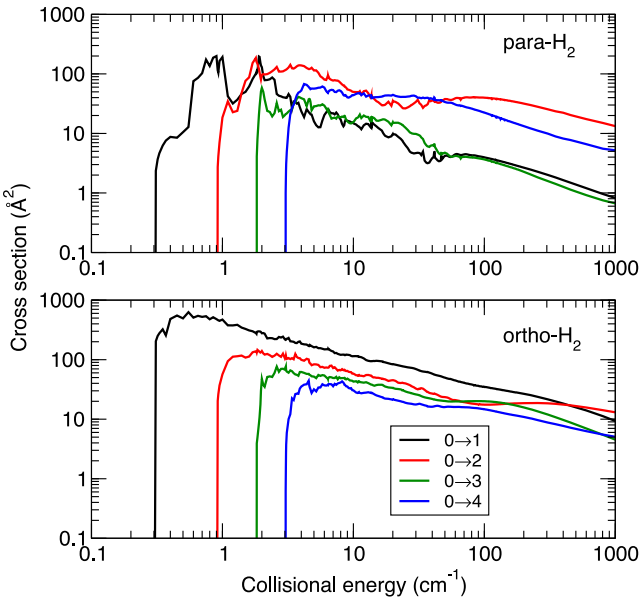

Figure 1. Cross-sections for rotational excitation out of the ground state of HC_3N $j_1 = 0$ into $j_1' = 1, 2, 3$ and 4 as function of collisional energy. Upper and lower panels correspond to collisions due to para-H_2($j_2 = 0$) and ortho-H_2($j_2 = 1$), respectively.

4 RESULTS

4.1 Collisional propensity rules

In Fig. 1, cross-sections for the rotational excitations $j_1 = 0 \rightarrow 1, 2, 3, 4$ are plotted as function of collision energy for the colliders para-H_2($j_2 = 0$) and ortho-H_2($j_2 = 1$). It is first noticed that these cross-sections show prominent resonances at low energies, especially in the case of para-H_2($j_2 = 0$). These resonances, of both shape and Feshbach types, arise from purely quantum effects. They have been observed experimentally only recently (see e.g. Chefdeville et al. 2012, 2015, in the case of CO–H_2). We also observe in the case of para-H_2($j_2 = 0$) that transitions with even Δj_1 (i.e. $\Delta j_1 = 2, 4$) have the largest cross-sections, with $\Delta j_1 = 4$ being even dominant in the energy range ∼15–45 cm^{-1}. This result was interpreted by Wernli et al. (2007a) as originating from the shape of the HC_3N–para-H_2 PES, being nearly a prolate ellipsoid. It should be noted that these results are unchanged when the basis set on H_2 include the $j_2 = 2$ level (see fig. 1 in Wernli et al. 2007b). In contrast, in the case of ortho-H_2, cross-sections follow an energy-gap law behaviour with $\Delta j_1 = 1 > \Delta j_1 = 2 > \Delta j_1 = 3$, etc. We note, still, that above ∼400 cm^{-1}, the transition $0 \rightarrow 2$ dominates.

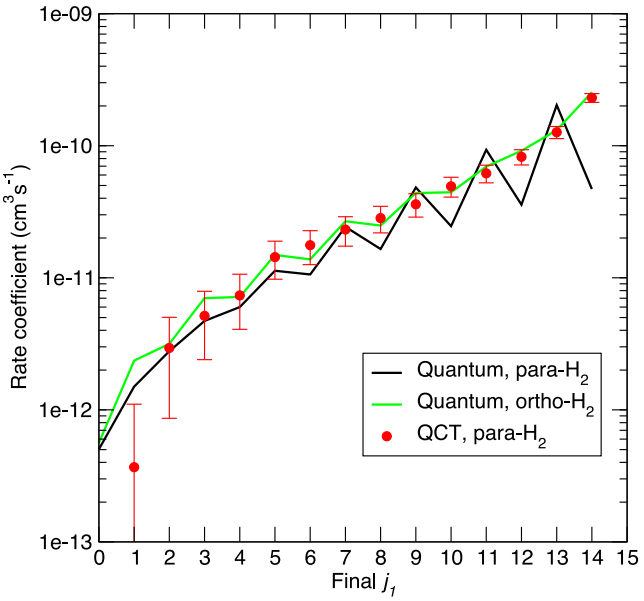

Figure 2. Rate coefficients for the HC_3N deexcitation $j_1 = 15 \rightarrow j_1'$ by H_2 at 100 K. Quantum coupled-channel results are given by the solid black and light green lines for para-$H_2(j_2 = 0)$ and ortho-$H_2(j_2 = 1)$, respectively. QCT results are represented by the solid circles with error bars representing two standard deviations.

These results illustrate clearly the difference between para- and ortho-H_2. It was previously observed for many other systems where the target has a large dipole, e.g. for HCN–H_2 (Vera et al. 2014). In the case of formaldehyde (H_2CO), it was even used to indirectly constrain the ortho-to-para ratio of H_2 (Troscompt et al. 2009). Indeed, the general distinction between para- and ortho-H_2 is attributable to the permanent quadrupole moment of H_2, which vanishes for $j_2 = 0$ but not for $j_2 > 0$. When the dipole of the target is significant, the long-range dipole-quadrupole interaction term is large and the difference between para-$H_2(j_2 = 0)$ and ortho-$H_2(j_2 = 1)$ is substantial (at the quantum level).

4.2 Comparison between classical and quantum rates

A comparison between quantum and classical rate coefficients is presented in Fig. 2 for HC_3N initially in level $j_1 = 15$. The kinetic temperature is fixed at 100 K and the rate coefficients are plotted as function of the final HC_3N level j_1'. We first notice that the quantum results for para-$H_2(j_2 = 0)$ show a pronounced even Δj_1 ('near homonuclear') propensity, as expected from the cross-sections reported above. This propensity is not observed at the QCT level whereas the PES are identical, demonstrating that this result indeed arises from a purely quantum effect. In fact, this propensity was explained semi-classically by McCurdy & Miller (1977) in terms of an interference effect related to the even anisotropy of the PES. Interferences are of course ignored in QCT calculations so that the 'zig-zags' are totally absent. Now when ortho-$H_2(j_2 = 1)$ is the projectile, the zig-zags are almost entirely suppressed and, interestingly, the quantum results are in excellent agreement with the QCT calculations, within error bars (except for the largest $\Delta j_1 = 14$ transfer). This demonstrates that the quadrupole moment of H_2, which vanishes for $H_2(j_2 = 0)$, plays a crucial role by breaking the even symmetry of the PES and suppressing the interference effect. But it does not modify the magnitude of the cross-sections, which are well reproduced by purely classical mechanics with para-$H_2(j_2 = 0)$. This result also suggests that the scattering process is dominated by the short-range part of the PES, i.e. by the ellipsoidal shape of the potential. It should be noted that the interference structure is extremely sensitive to the PES anisotropy and rotationally state-selected experiments which resolve this structure would provide a critical test of theory (see e.g. Carty et al. 2004, in the case of CO+He).

These results show that QCT calculations can be employed with confidence to mimic collisions with rotationally excited $H_2(j_2 \geq 1)$. They should be reliable to within 10–30 per cent for rate coefficients larger than $\sim 10^{-12}$ cm^{3}s^{-1}. Smaller rate coefficients have much larger uncertainties because they correspond to *rare* or 'classically forbidden' transitions with small probabilities.

4.3 Thermalized rate coefficients

The ortho-to-para ratio of H_2 can be out of thermal equilibrium in the ISM (e.g. Faure et al. 2013, and references therein). It is thus crucial to consider the two nuclear spin species of H_2 as two separate colliders. We can however generally assume that each nuclear spin species has a thermal distribution of rotational levels. At temperatures below ~80 K, only the ground states are significantly populated so that in practice only para-$H_2(j_2 = 0)$ and ortho-$H_2(j_2 = 1)$ must be considered. At higher temperatures, however, the levels $j_2 = 2$, 3 and 4 also play an important role because their (thermal) populations become larger than 1 per cent above ~80 K, ~160 K and ~260 K, respectively. Due to the prohibitive CPU cost, we did not perform extensive scattering calculations for these excited levels but a few energy points were computed. We have thus found that rotational cross-sections for H_2 initially in $j_2 = 2$ differ by less than ~ 20–30 per cent with those for H_2 in $j_2 = 1$. As a result, it can be assumed that all cross-sections, and by extension all rate coefficients, for $H_2(j_2 > 1)$ are identical to those for $H_2(j_2 = 1)$. This result was observed previously for many other systems, as a rather general rule (e.g. Daniel et al. 2014, and references therein). We note that at higher temperatures where the H_2 levels can be (de)excited, this rule holds for 'effective' rate coefficients which are summed over the final H_2 levels.

For para-H_2, we have thus computed the 'thermalized' rate coefficients by weighting the para-$H_2(j_2 = 0)$ rate coefficients, $k_{j_1, j_2=0 \rightarrow j_1'}(T)$,[2] by the thermal distribution of the $j_2 = 0$ level and the ortho-$H_2(j_2 = 1)$ rate coefficients, $k_{j_1, j_2=1 \rightarrow j_1'}(T)$, by the thermal distribution of all para levels with $j_2 > 0$:

$$k_{j_1, p\mathrm{H}_2 \rightarrow j_1'}(T) = \rho_0 k_{j_1, j_2=0 \rightarrow j_1'}(T) + (1 - \rho_0) k_{j_1, j_2=1 \rightarrow j_1'}(T), \quad (2)$$

where

$$\rho_0 = \frac{1}{\sum_{j_2=0,2,4,\ldots}(2j_2 + 1)\exp(-E_{j_2}/k_B T)} \quad (3)$$

is the thermal population of $j_2 = 0$.

For ortho-H_2, all H_2 levels were assumed to have the same rate coefficients so that the 'thermalized' rate coefficients were simply obtained as:

$$k_{j_1, o\mathrm{H}_2 \rightarrow j_1'}(T) = k_{j_1, j_2=1 \rightarrow j_1'}(T). \quad (4)$$

In Fig. 3, the thermalized rate coefficients for para-H_2 and ortho-H_2 are plotted as function of temperature for the ground-state transition $j_1 = 1 \rightarrow 0$ at 9.1 GHz. The contribution of $j_2 = 2$ is significant

[2] Since rotational transitions in H_2 are neglected in our calculations, the calculated rate coefficients are 'effective' and the final H_2 level j_2' can be omitted from the notation.

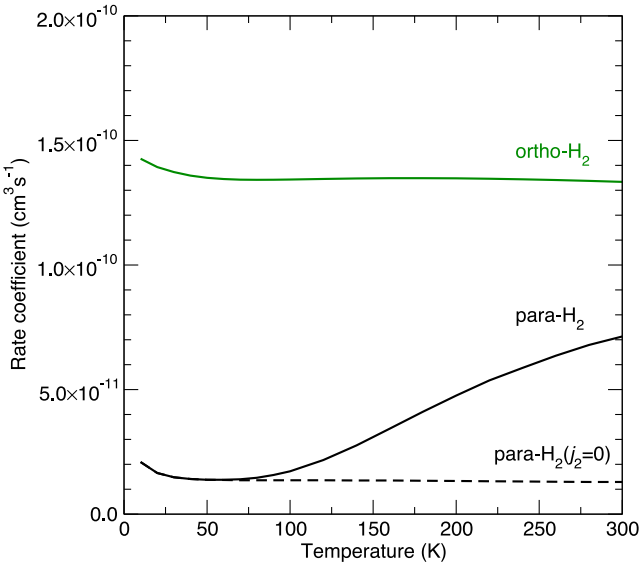

Figure 3. Rate coefficients for the HC_3N deexcitation $j_1 = 1 \rightarrow 0$ by para-H_2 and ortho-H_2 in the temperature range 10–300 K. The thermalized rate coefficient for para-H_2($j_2 = 0$, 2, 4, ...) is compared to the contribution of the ground state $j_2 = 0$.

above ∼80 K, as expected, and it is here amplified by the fact that the corresponding rate coefficient (set equal to $k_{j_1,j_2=1\rightarrow j_1'}(T)$) is about a factor of 10 larger than $k_{j_1,j_2=0\rightarrow j_1'}(T)$ (see equation 2). At 300 K, the contribution of $j_2 = 2$ (and to much a lesser extent $j_2 = 4$) increases the rate coefficient of para-H_2 by a factor of ∼6. It is therefore of crucial importance at these temperatures.

The whole set of thermalized rate coefficients for the lowest 38 rotational levels of HC_3N and kinetic temperatures in the range 10–300 K are available at the LAMDA[3] (Schöier et al. 2005) and BASECOL[4] (Dubernet et al. 2013) data bases. We note that for HC_3N levels between $j_1 = 31$ and $j_1 = 37$, only QCT rate coefficients for para-H_2($j_2 = 0$) are available and no thermal averaging was applied to this set which is employed for both para-H_2 and ortho-H_2.

4.4 Hyperfine cross-sections and rate coefficients

In order to evaluate the accuracy of the S-IOS method (see Section 3.3) in the case of HC_3N–H_2 collisions, we have computed recoupling and S-IOS hyperfine cross-sections at two selected collisional energies (10 and 50 cm^{-1}). In the above equation (1), cross-sections were employed instead of rate coefficients. Fig. 4 shows a comparison between recoupling and S-IOS hyperfine cross-sections for all the de-excitation transitions from the initial level $j_1 = 5$, including quasi-elastic transitions (those with $j_1 = j_1'$ and $F_1 \neq F_1'$), for collisions with para-H_2($j_2 = 0$) and ortho-H_2($j_2 = 1$). We note that the S-IOS approach imposes selection rules (through Wigner 6j symbols) and some cross-sections (not plotted) are strictly zero. The corresponding transitions are those between the ($j_1 = 1$, $F_1 = 0$) level and levels with $F_1 = j_1$, e.g. (1, 0) → (1, 1). At the close-coupling level, these transitions have indeed cross-sections lower than ∼1 Å^2.

For collisions with para-H_2($j_2 = 0$), the agreement between recoupling and S-IOS calculations is very satisfactory. At low energies, the differences between the two sets of data are less than 20–30 per cent (especially for the dominant cross-sections). At kinetic energies greater than 50 cm^{-1}, cross-sections are almost identical. We conclude that the S-IOS approach can be used with confidence to compute hyperfine rate coefficients in the case of collisions with para-H_2($j_2 = 0$). For collisions with ortho-H_2($j_2 = 1$), the agreement between recoupling and S-IOS calculations is less satisfactory. At low energies, the two sets of data agree within a typical factor of 3. At kinetic energies greater than 50 cm^{-1}, the differences between the two sets decrease and the average difference is lower than a factor of 2.

To summarize, the S-IOS method can provide hyperfine resolved rate coefficients with an average accuracy better than 20–30 per cent in the case of collisions with para-H_2($j_2 = 0$) and within a factor of 2–3 in the case of collisions with ortho-H_2($j_2 = 1$). With respect to the memory and CPU cost of full recoupling calculations, the S-IOS approximation therefore represents a suitable (and low-cost) alternative for this system. Finally, in terms of radiative transfer application, it should be noted that at moderate and high opacities, where the relative hyperfine populations can significantly depart from the statistical weights, the S-IOS method is notably better than the statistical approach (see Faure & Lique 2012).

In practice, hyperfine resolved rate coefficients were obtained for the lowest 61 hyperfine levels of HC_3N, i.e. up to ($j_1 = 20$, $F_1 = 20$) which lies 63.73 cm^{-1} above (0, 1), and for kinetic temperatures in the range 10–100 K. This set of data is available at the LAMDA and BASECOL data bases.

5 CONCLUSION

We have reported in this paper rate coefficients for the rotational excitation of HC_3N by para- and ortho-H_2. The lowest 38 rotational levels of HC_3N were included and kinetic temperatures up to 300 K were considered. The scattering calculations were performed at the quasi-classical and quantum coupled-channel level using the interaction potential of Wernli et al. (2007a). This potential was also employed to compute the bound-states of the complex in order to make comparisons with the spectroscopy measurements of M11. Theory and experiment were found to agree within 0.5 per cent for para-H_2($j_2 = 0$) and within a few per cent for ortho-H_2($j_2 = 1$), demonstrating the high accuracy of the potential. It appears from these comparisons that the calculated state-to-state rotational rate coefficients are likely to be accurate to about 20–30 per cent. Hyperfine resolved rate coefficients were also deduced using the S-IOS approximation, with a somewhat lower accuracy. The whole set of data represent a significant improvement and extension over the previous data of Green & Chapman (1978) and Wernli et al. (2007a).

The next step is to determine a flexible potential energy surface in order to treat the ro-vibrational excitation of HC_3N. The lowest vibrational state is the ν_7 bending mode which lies at 222 cm^{-1} above the ground vibrational state. Ro-vibrational excitation due to collisions is therefore expected to play a role above ∼300 K. Such calculations are highly challenging due to excessively large number of channels involved. This problem has been however tackled recently at the quantum coupled-channel level using the rigid-bender approximation (Stoecklin et al. 2013; Stoecklin, Denis-Alpizar & Halvick 2015). This latter approximation was also employed previously in quasi-classical trajectories (Faure et al. 2005) which offer an (economical) alternative to quantum computations, as shown in this work.

In summary, this set of data, possibly complemented by electron-impact rate coefficients (as given in Gratier et al. 2013), should

[3] http://www.strw.leidenuniv.nl/∼moldata
[4] http://basecol.obspm.fr

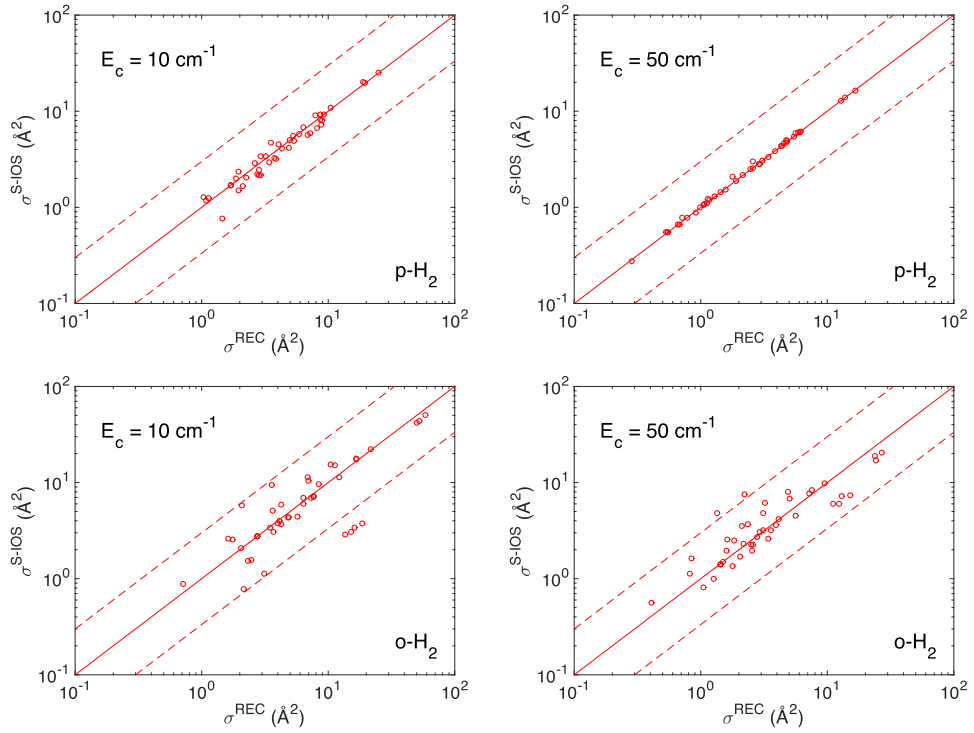

Figure 4. Comparison between HC_3N–H_2 recoupling and S-IOS hyperfine cross-sections for all the de-excitation transitions from $j_1 = 5$ at two different collisional energies. The vertical axis represents the hyperfine S-IOS cross-sections and the horizontal axis represents the corresponding hyperfine recoupling cross-sections. The two dashed lines in each panel delimit the region where the cross-sections differ by less than a factor of 3.

help in modelling non-LTE HC_3N spectra in cold to warm regions of the ISM. We note in particular that HC_3N has recently been detected in protopolanetary discs (Chapillon et al. 2012; Öberg et al. 2015). The collisional data provided here should prove very useful in interpreting such observations.

ACKNOWLEDGEMENTS

This research was supported by the CNRS national programme 'Physique et Chimie du Milieu Interstellaire'. Most of the computations presented in this paper were performed using the CIMENT infrastructure (https://ciment.ujf-grenoble.fr), which is supported by the Rhône-Alpes region (GRANT CPER07 13 CIRA).

REFERENCES

Bockelée-Morvan D. et al., 2000, A&A, 353, 1101
Carty D., Goddard A., Sims I. R., Smith I. W. M., 2004, J. Chem. Phys., 121, 4671
Chapillon E. et al., 2012, ApJ, 756, 58
Chapman S., Green S., 1977, J. Chem. Phys., 67, 2317
Chefdeville S., Stoecklin T., Bergeat A., Hickson K. M., Naulin C., Costes M., 2012, Phys. Rev. Lett., 109, 023201
Chefdeville S., Stoecklin T., Naulin C., Jankowski P., Szalewicz K., Faure A., Costes M., Bergeat A., 2015, ApJ, 799, L9
Daniel F., Faure A., Wiesenfeld L., Roueff E., Lis D. C., Hily-Blant P., 2014, MNRAS, 444, 2544
Denis-Alpizar O., Kalugina Y., Stoecklin T., Vera M. H., Lique F., 2013, J. Chem. Phys., 139, 224301
Dubernet M.-L. et al., 2013, A&A, 553, A50
Faure A., Lique F., 2012, MNRAS, 425, 740
Faure A., Wiesenfeld L., Wernli M., Valiron P., 2005, J. Chem. Phys., 123, 104309
Faure A., Hily-Blant P., Le Gal R., Rist C., Pineau des Forêts G., 2013, ApJ, 770, L2
Gratier P., Pety J., Guzmán V., Gerin M., Goicoechea J. R., Roueff E., Faure A., 2013, A&A, 557, A101
Green S., Chapman S., 1978, ApJS, 37, 169
Hutson J. M., 1994, Comput. Phys. Commun., 84, 1
Hutson J. M., Green S., 1995, Molscat Computer Code, version 14. Daresbury Laboratory, Warington, UK
Jankowski P., McKellar A. R. W., Szalewicz K., 2012, Science, 336, 1147
Lanza M., Lique F., 2014, J. Chem. Phys., 141, 164321
McCurdy C. W., Miller W. H., 1977, J. Chem. Phys., 67, 463
Michaud J. M., Topic W. C., Jäger W., 2011, J. Phys. Chem. A, 115, 9456 (M11)
Morris M., Turner B. E., Palmer P., Zuckerman B., 1976, ApJ, 205, 82
Neufeld D. A., Green S., 1994, ApJ, 432, 158
Öberg K. I., Guzmán V. V., Furuya K., Qi C., Aikawa Y., Andrews S. M., Loomis R., Wilner D. J., 2015, Nature, 520, 198
Orgel L. E., 2002, Orig. Life Evol. Biosph., 32, 279
Schöier F. L., van der Tak F. F. S., van Dishoeck E. F., Black J. H., 2005, A&A, 432, 369
Stoecklin T., Denis-Alpizar O., Halvick P., Dubernet M.-L., 2013, J. Chem. Phys., 139, 124317
Stoecklin T., Denis-Alpizar O., Halvick P., 2015, MNRAS, 449, 3420
Troscompt N., Faure A., Maret S., Ceccarelli C., Hily-Blant P., Wiesenfeld L., 2009, A&A, 506, 1243
Turner B. E., 1971, ApJ, 163, L35
Vera M. H., Kalugina Y., Denis-Alpizar O., Stoecklin T., Lique F., 2014, J. Chem. Phys., 140, 224302
Wernli M., 2006, PhD Thesis, Université Joseph Fourier
Wernli M., Wiesenfeld L., Faure A., Valiron P., 2007a, A&A, 464, 1147
Wernli M., Wiesenfeld L., Faure A., Valiron P., 2007b, A&A, 475, 391

This paper has been typeset from a TEX/LATEX file prepared by the author.